Macromolecules

Article

pubs.acs.org/Macromolecules

Ionic Conduction in Poly(ethylene glycol)-Functionalized Hexa-*peri*-hexabenzocoronene Amphiphiles

Achilleas Pipertzis,[†] George Zardalidis,[†] Katrin Wunderlich,[‡] Markus Klapper,[‡] Klaus Müllen,[‡] and George Floudas*[,†]

[†]Department of Physics, University of Ioannina, P.O. Box 1186, 451 10 Ioannina, Greece

[‡]Max Planck Institute for Polymer Research, 55128 Mainz, Germany

Supporting Information

ABSTRACT: Discotic liquid crystals based on hexa-*peri*-hexabenzocoronenes (HBCs) symmetrically substituted with six poly(ethylene glycol) (PEG) chains and further doped with $LiCF_3SO_3$ (LiTf) salt at different [EG]:[Li^+] ratios nanophase-separate in domains composed from HBC columns and PEG chains. These model amphiphiles behave as viscoelastic solids with a shear modulus of 5×10^6 Pa and an ionic conductivity of 10^{-5} S/cm at 373 K. At temperatures below 333 K an ionic superstructure is formed of higher shear modulus (10^8 Pa) that surrounds the HBC columns and follows the disks in their rotational motion. However, the ionic superstructure impedes ion transport. Substituting the HBC core with two PEG chains breaks the symmetry of the ionic superstructure and increases ionic conductivity by an order of magnitude while retaining a high shear modulus and a viscoelastic response. These findings demonstrate that PEG-functionalized HBCs have great potential as new electrolytes because they combine ionic conductivity with mechanical stability. Moreover, when combined with electronic conduction within the HBC columns, this design can result in structures that exhibit simultaneous electronic and ionic transport.

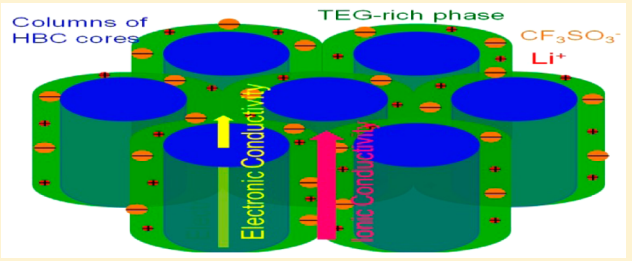

I. INTRODUCTION

In recent years there has been considerable interest in materials which conduct both electronic charge and ions on the nanometer length scales. Earlier studies concentrated on inorganic[1,2] and more recent studies on organic materials.[3−6] The latter were based on mixtures of lamella-forming poly(3-hexylthiophene)-*b*-poly(ethylene oxide) (P3HT-*b*-PEO) block copolymers with a lithium salt.[5,6] In this case, the lithium salt was found in both P3HT and PEO nanophases and ionic conductivity was some orders of magnitude higher than the electronic conductivity. Other possible candidates for such materials are based on liquid crystals (LC). Recent studies explored the possibility of using liquid crystal ion-conducting materials for energy storage devices such as lithium batteries.[7−10] Discotic liquid crystals (DLCs), in particular, constitute a class of organic semiconductors with applications in organic field-effect transistors and photovoltaic cells. Applications of DLCs in nanoscale conductive devices rely on the optimal stacking of the aromatic cores that allows for charge carrier mobility along the columnar axis (molecular wires).[11] Hexabenzocoronenes (HBCs) with the large conjugated core are an important class of DLCs.[12−18] Within their columnar phases, molecules are stacked one on top of each other forming columns that are further organized in a two-dimensional lattice. X-ray scattering revealed two main columnar structures in HBCs: First, a liquid crystalline phase (Col_h) at higher temperatures composed of columns that are further organized in a hexagonal lattice. Second, a crystalline phase (C_r) at lower temperatures composed of columns of tilted disks (i.e., "herringbones") in a monoclinic unit cell. Extensive structural,[19,20] kinetic,[21,22] and dynamic[23,24] experiments in a series of dipole-functionalized HBCs revealed that the two phases possess not only distinctly different unit cells but also different dipolar and viscoelastic signatures. Furthermore, confinement within rigid nanopores furnished arrays of 1D supramolecular wires with uniform columnar orientation on a macroscopic scale suitable to generate supramolecular 1D wires for electronic charge transport.[25]

Coaxial structures based on HBC cores decorated with short PEG chains[26,27,18] when doped with electronic charge and lithium ions, respectively, offer a unique possibility for electronic *and* ionic conducting pathways. The long-term aim of our research is the design of coaxial structures composed of electronically conducting, yet ionically insulating, columnar structures (HBC) surrounded by an electronically insulating, yet ionically conducting phase (PEG). Herein we explore mainly ionic conduction based on doping of HBC-PEG with $LiCF_3SO_3$ (LiTf) and provide some preliminary results on electronic conduction in the same systems. The choice of PEG as the ion-conducting pathway is straightforward: PEG is a flexible polymer with high solvating capability for a number of lithium salts and at the same time is biodegradable and

Received: January 31, 2017
Revised: February 23, 2017

DOI: 10.1021/acs.macromol.7b00224
Macromolecules XXXX, XXX, XXX−XXX

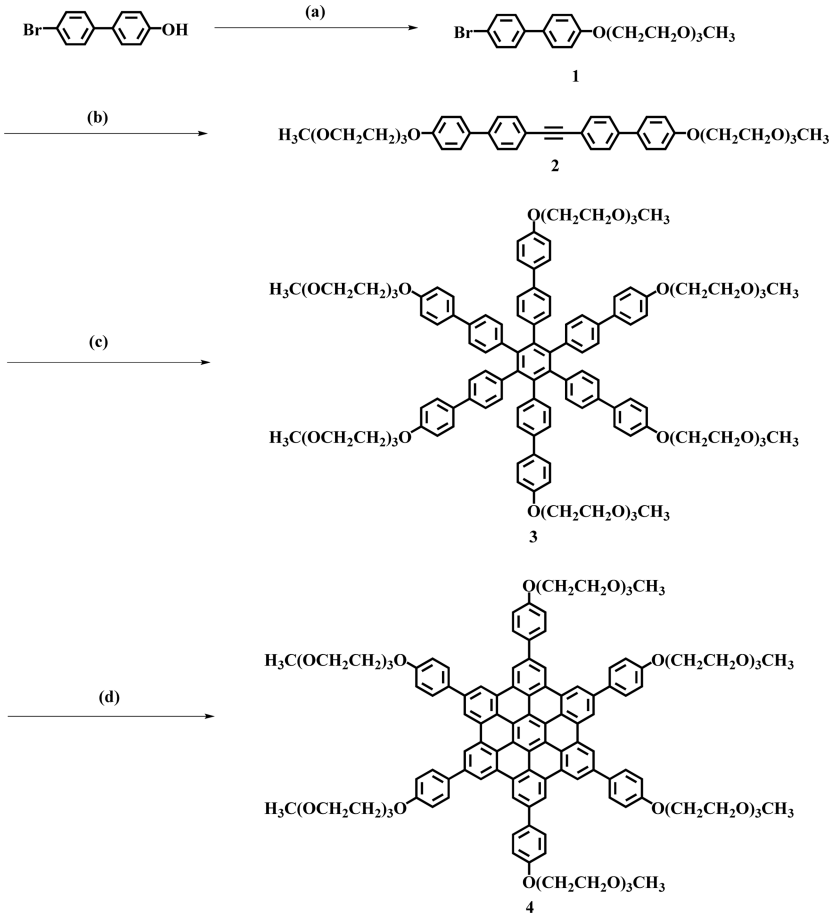

Figure 1. Synthetic scheme for HBC-TEG$_6$ (**4**): (a) TsO$(CH_2CH_2O)_3CH_3$, K_2CO_3, DMF, 80 °C, 24 h; (b) TMS-acetylene, $PdCl_2(PPh_3)_2$, CuI, DBU, benzene, H_2O, 60 °C, 24 h; (c) $[Co_2(CO)_8]$, dioxane, reflux; 12 h (58%); (d) $FeCl_3$, CH_3NO_2, DCM, 20 °C, 5 h (95%).

environmentally friendly.[28] However, PEG is lacking the necessary mechanical stability and high elastic modulus[29] necessary to prevent dendritic growth at the electrodes, a key issue in battery applications.[30] This fact has initiated the pursue of effective scaffolds for PEO electrolytes based on more stiff macromolecules. Hence, PEG has been "combined" with stiffer macromolecules, as for example in block copolymers with poly(styrene-*b*-ethylene oxide) (PS-*b*-PEO) being the most studied copolymer. Here the hard nanophase (PS) provides the required elastic modulus and the soft phase (PEG) supports ion conduction.[31−39]

We have recently investigated Li ion conduction in propeller-shaped hexaphenylbenzenes (HPB) substituted with PEG chains and doped with LiTf.[40] A unique feature of the latter system was the Vogel−Fulcher−Tammann temperature dependence of dc conductivity with values that were comparable to the archetypical polymer electrolyte PEG/LiTf.[29] However, HPBs cannot be employed as efficient scaffolds as they lack the required mechanical stability. In the present work the scaffold for the PEG electrolytes is provided by the rigid HBC columnar structures. To our knowledge, this is the first time that HBCs are used as scaffolds for Li ion conductivity. HBC-PEG/LiTf with a range of electrolyte concentrations (with ratio [EO]:[Li^+] = 3:1, 8:1, and 12:1) was investigated with respect to the thermal properties, self-assembly, mechanical stability, and Li-ion conductivity. These model amphiphiles are viscoelastic solids with a high shear modulus (with values in the range from 5×10^6 to 10^8 Pa) over a broad temperature range. Our results demonstrate that LiTf is located exclusively in the PEG nanophase and has an ionic conductivity of 10^{-5} S/cm at 373 K. We explore the role of ions (a) in stabilizing a certain unit cell and (b) in creating an ionic superstructure that surrounds the HBC columns. The role of the latter regarding the mechanical stability and ionic conductivity is discussed. Furthermore, we explore the effect of asymmetric PEG functionalization of the HBC core on the self-assembly and ionic conductivity. We find that asymmetric substitution results in a further increase of ionic conductivity by an order of magnitude.

II. EXPERIMENTAL SECTION

Materials and Methods. Unless otherwise noted, all starting materials were purchased from Sigma-Aldrich, Acros, ABCR, and Alfa Aesar and used as received without further purification. Synthesis was carried out under inert atmosphere using anhydrous solvents. For reactions performed at higher temperatures, the given temperature refers to the temperature of the oil bath used for heating. Column chromatography for purification purposes was performed with silica gel (particle size 0.063−0.200 mm from Merck) and for analytic thin layer chromatography on silica-coated aluminum sheets with fluorescence indicator from Macherey-Nagel. Synthesis of compounds **1** and **2** has been reported in the literature[18] as well as the preparation of compound **6**.[41]

Measurements. ^1H and ^{13}C NMR spectroscopies were carried out with Bruker AMX 300 (300 MHz) and Bruker DRX 700 (700 MHz). MALDI-TOF was performed on a Bruker Daltonic Reflex machine that was calibrated using a fullerene mixture (Sigma-Aldrich, CAS 131159-39-2) with dichloromethane as solvent and dithranol as matrix

DOI: 10.1021/acs.macromol.7b00224
Macromolecules XXXX, XXX, XXX−XXX

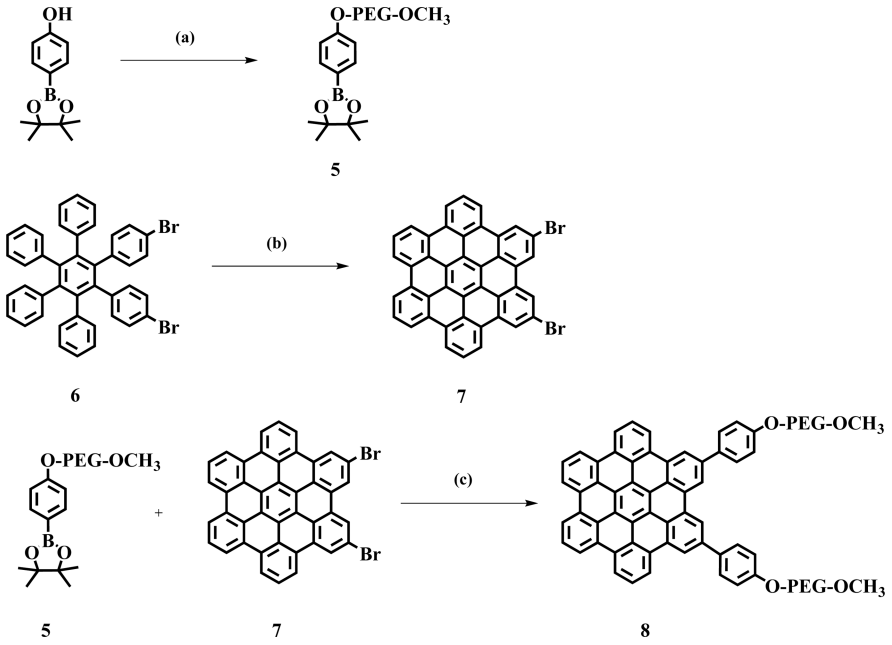

Figure 2. Synthesis of HBC containing two PEG chains (**8**): (a) K_2CO_3, acetone, 18 h, 80 °C; (b) 2,3-dichloro-5,6-dicyano-*p*-benzoquinone (DDQ), trifluoromethanesulfonic acid, dichloromethane, 2 h, RT, 95%; (c) [$Pd(PPh_3)_4$], tetraethylammonium hydroxide, toluene, 90 °C, 16 h.

or solvent-free and tetracyanoquinodimethane (TCNQ) as matrix. Elemental composition (C, H, N) was analyzed with a Foss HeraeusVario EL machine (Analytic Laboratory, Institute of Organic Chemistry, Johannes Gutenberg University Mainz). The optical absorption measurements were performed at ambient temperature using a UV/vis/NIR PerkinElmer Lambda 9 spectrometer. The molecular weights and molecular weight distributions were determined by means of gel permeation chromatography (GPC) with THF as eluent (1 mL/min) at 30 °C. The instrument was equipped with a refractive index (RI) detector (ERCRI-101 differential refractometer detector) and fitted with a PSS-SDV 300 × 8 mm, particle size 10 μm, and pore size 500, 10^5, and 10^6 Å. The molecular weights were determined from a calibration curve based on linear poly(styrene) standards.

*Synthesis of HBC-TEG$_6$ (**4**).* The synthesis of HBC-TEG$_6$ is displayed in Figure 1. The synthesis of HBC-TEG$_6$ (**4**) was performed using etherification chemistry and continuing with a Sonogashira reaction to generate a diphenylacetylene derivative (**2**). Subsequent cyclotrimerization[42] of , catalyzed by [$Co_2(CO)_8$] afforded compound **3**. The amphiphilic discotic molecule HBC-TEG$_6$ (**4**) was obtained by oxidative cyclo-dehydrogenation with a solution of $FeCl_3$ in nitromethane.

*Synthesis of HBC with Two PEG Chains (**8**).* HBC with two PEG chains (**8**) was prepared as shown in Figure 2. 4-(4,4,5,5-Tetramethyl-1,3,2-dioxaborolan-2-yl)phenol was first subjected to etherification with α-methoxy-ω-bromo-PEG (M_n(PEG) = 750 g/mol, M_w/M_n = 1.01). Oxidative cyclo-dehydrogenation of 4,4″-dibromo-3′,4′,5′,6′-tetraphenyl-1,1′:2′,1″-terphenyl (**6**) led to 2,5-dibromohexabenzo[*bc*,*ef*,*hi*,*kl*,*no*,*qr*]coronene (**7**). Then HBC with two PEG chains (**8**) was synthesized with a palladium-catalyzed Suzuki coupling of compounds **5** and **7**. To remove the Pd catalyst, HBC with two PEG chains was washed several times with water and extracted with dichloromethane. After size exclusion chromatography, **8** was obtained as a pure yellow oil.

According to GPC and MALDI-TOF analysis, a small amount of PEG and byproducts such as HBC with one PEG chain were formed after the Suzuki reaction. The removal of these impurities was achieved by preparative GPC. The resulting molecules (**5**–**8**) were characterized by ^{1}H and ^{13}C NMR spectroscopy and MALDI-TOF mass spectrometry. Molecules **5** and **8** were further characterized by GPC. In addition to the HBC-TEG$_6$/LiTf mixtures, triethylene glycol dimethyl ether with lithium triflate mixtures at the same compositions were prepared—and used as reference points for the conductivity—as described in the Supporting Information. Further details on the synthesis and characterization are provided in the Supporting Information (Figures S1–S7).

Differential Scanning Calorimetry. The thermodynamic state of the neat compounds **4** and **8** as well as after doping with LiTf was studied by differential scanning calorimetry (DSC) with a Q2000 (TA Instruments). The instrument was calibrated for best performance in the specific temperature range and heating/cooling rate. The calibration sequence included a baseline calibration for the determination of the time constants and capacitances of the sample and reference sensor using a sapphire standard, an enthalpy and temperature calibration for the correction of thermal resistance using indium as standard (ΔH = 28.71 J/g, T_m = 428.8 K), and a heat capacity calibration with sapphire standard. Measurements were made on cooling and subsequent heating at a rate of 5 K/min. The DSC traces of compounds **4** and **8** from the second heating scans are shown in Figures 3 and 12, respectively. The traces reveal a very different thermodynamic state in the two compounds.

Polarizing Optical Microscopy (POM). A Zeiss Axioskop 40 equipped with a video camera and a fast frame grabber was used to follow the structural changes of the two samples. The samples were prepared between two Linkam glass microscopy slides with a distance of 25 μm maintained by Teflon spacers. A Linkam temperature control unit (THMS600), equipped with a TMS94 temperature programmer, was employed for the temperature-dependent studies. Images were recorded following slow cooling (1 °C/min) from the isotropic state.

X-ray Scattering. Wide-angle X-ray scattering (WAXS) measurements were made using Cu Kα radiation from a RigakuMicroMax 007 X-ray generator (λ = 1.541 84 nm), using Osmic Confocal Max-Flux curved multilayer optics. Samples in the form of fibers were prepared with a mini-extruder at 303 K. Temperature-dependent WAXS measurements were performed by inserting the fibers into glass capillaries (1 mm diameter) at temperatures in the range from 298 to 393 K in steps of 10 K. A waiting (equilibration) time of 1800 s and a measurement time of 3600 s were set in the temperature program. Diffraction patterns were obtained by radial averaging of the data recorded by a 2D detector (Mar345 Image Plate).

Dielectric Spectroscopy. Dielectric spectroscopy (DS) measurements were performed with a Novocontrol Alpha frequency analyzer as a function of temperature. Measurements were recorded at different temperatures in the range from 203 to 413 K in steps of 5 K for

DOI: 10.1021/acs.macromol.7b00224
Macromolecules XXXX, XXX, XXX–XXX

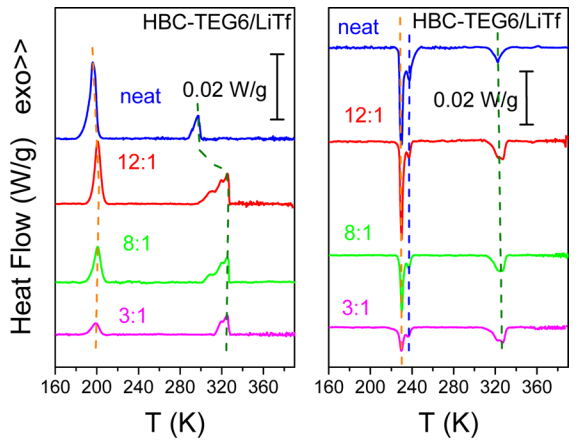

Figure 3. DSC traces of neat HBC-TEG6 (**4**) (blue) and of the same HBC-TEG6 doped with $LiCF_3SO_3$ at different salt concentrations [EO]:[Li^+] = 12:1 (red), 8:1 (green), and 3:1 (magenta). Traces are obtained during the second cooling (left) and the second heating run (right) with a rate of 5 K/min. Traces are shifted vertically for clarity.

frequencies in the range from 10^{-2} to 10^7 Hz. The complex dielectric permittivity $\varepsilon^* = \varepsilon' - i\varepsilon''$, where ε' is the real and ε'' is the imaginary part, has been obtained as a function of frequency ω and temperature T i.e., $\varepsilon^*(T,\omega)$.[43−45] The analysis of the T-dependent experiments was made using the empirical equation of Havriliak and Negami (HN):[46]

$$\varepsilon^*_{HN}(\omega, T) = \varepsilon_\infty(T) + \frac{\Delta\varepsilon(T)}{[1 + (i\omega\tau_{HN}(T))^m]^n} + \frac{\sigma_0(T)}{i\varepsilon_f\omega} \quad (1)$$

where $\varepsilon_\infty(T)$ is the high-frequency permittivity, $\tau_{HN}(T)$ is the characteristic relaxation time in this equation, $\Delta\varepsilon(T) = \varepsilon_0(T) - \varepsilon_\infty(T)$ is the relaxation strength, m and n (with limits $0 < m, mn \leq 1$) describe respectively the symmetrical and asymmetrical broadening of the distribution of relaxation times, σ_0 is the dc conductivity, and ε_f is the permittivity of free space. From τ_{HN}, the relaxation time at maximum loss, τ_{max}, is obtained analytically following

$$\tau_{max} = \tau_{HN} \sin^{-1/m}\left(\frac{\pi m}{2(1+n)}\right) \sin^{1/m}\left(\frac{\pi mn}{2(1+n)}\right) \quad (2)$$

In addition to the measured ε'' spectra, the derivative of ε' ($d\varepsilon'/d \ln \omega \sim -(2/\pi)\varepsilon''$) has been used in the analysis of the dynamic behavior. The characteristic time of ion mobility is obtained from the crossing of the real and imaginary parts of ε^* or, equivalently, of the modulus (M^*) representation ($\varepsilon^* = 1/M^*$).

III. RESULTS AND DISCUSSION

Thermodynamic State. The thermodynamic transitions of the neat compound HBC-TEG6 (compound **4**) are depicted in the DSC traces of Figure 3. The thermogram depicts two exothermic peaks on cooling at ∼300 and ∼200 K, suggesting two first-order phase transitions. On heating, there is hysteresis and the low-temperature endothermic peak now appears at ∼230 K, while the high-temperature peak at 323 K. The low-temperature feature most likely involves a phase transition from the crystalline phase to a liquid crystalline phase. The transition at higher temperatures involves a change in the unit cell from rhombohedral to hexagonal within the liquid crystalline phase (see below with respect to the WAXS investigation). In HBC-TEG6 doped with LiTf with salt concentrations [EO]:[Li^+] = 12:1, 8:1, and 3:1, the low-temperature first-order transition remains intact. However, there are differences in the high-temperature transition which on cooling now appears at ∼320 K, e.g., 20 K higher than in the neat compound **4**. As will be seen below, this transition does not relate to a change in the unit cell—as in bulk—but associates with the formation/melting of an ionic superstructure.

Self-Assembly. Information on the morphology is obtained by WAXS. Figures 4 and 5 refer to the self-assembly in neat

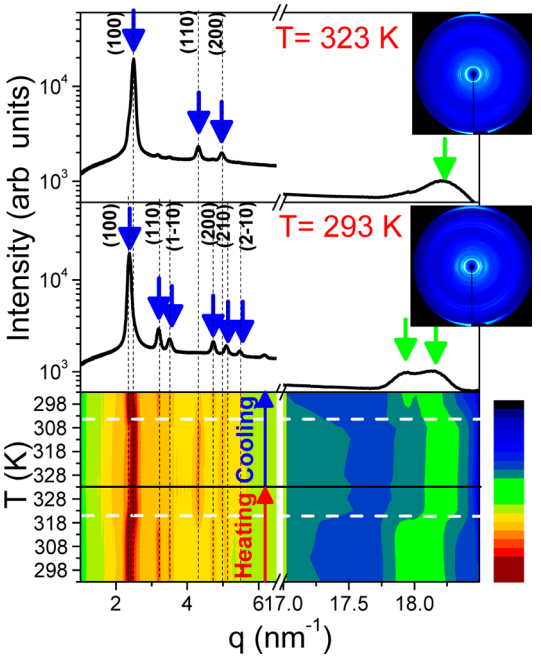

Figure 4. WAXS patterns of neat HBC-TEG6 at two temperatures, at 323 K (top) and at 293 K (middle) during heating. 2D-WAXS images from extruded HBC-TEG6-neat fibers at the respective temperatures are also depicted. (bottom) WAXS intensity contour plots during heating are also depicted. Blue and green arrows indicate the main equatorial and meridional reflections, respectively. Dashed lines give the position and (hkl) indices of the Bragg reflections from the hexagonal lattice (top) and rhombohedral lattice (middle). The horizontal white dashed lines depicted in the contour plot indicates the change of unit cell.

HBC-TEG6 and in HBC-TEG6 doped with LiTf at [EO]:[Li^+] = 8:1, respectively. The WAXS pattern of the neat compound **4** at 293 K reveals a set of equatorial reflections that correspond to the (100), (110), (1−10), (200), (210), and (2−10) reflections belonging to a rhombohedral unit cell with interplanar spacings, d_{hkl}, of the (hkl) lattice planes given by

$$\frac{1}{d_{hkl}^2} = \frac{(h^2 + k^2 + l^2)\sin^2\gamma + 2(hk + kl + hl)(\cos^2\gamma - \cos\gamma)}{\alpha^2(1 - 3\cos^2\gamma + 2\cos^3\gamma)} \quad (3)$$

The corresponding unit cell parameters are $a = b = 2.66$ nm and $\gamma = 85.2°$. At higher temperatures, the equatorial reflections have ratios of $1:3^{1/2}:4^{1/2}$ relative to the main peak and are associated with the (100), (110), and (200) reflections from a hexagonal unit cell. The spacings, d_{hkl}, now are related with the unit cell parameter a (=2.92 nm) as

$$\frac{1}{d_{hkl}^2} = \frac{4}{3}\frac{(h^2 + hk + k^2)}{a^2} \quad (4)$$

Furthermore, the transition temperatures from the rhombohedral to the hexagonal unit cells (indicated with the dashed horizontal lines in the intensity contour plots of Figure 4) are in

DOI: 10.1021/acs.macromol.7b00224
Macromolecules XXXX, XXX, XXX−XXX

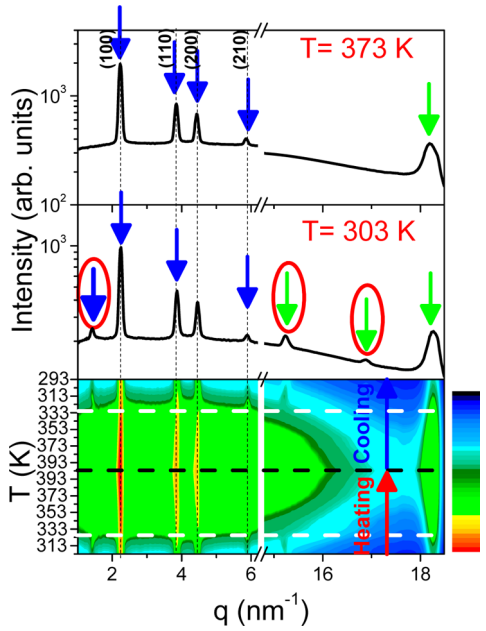

Figure 5. WAXS patterns of HBC-TEG6/LiTf with [EO]:[Li$^+$] = 8:1 at two temperatures, at 373 K (top) and at 303 K (middle) during heating. (bottom) WAXS intensity contour plot during heating are also depicted. The blue and green arrows indicate the main equatorial reflections and the main meridional reflections, respectively. Dashed lines give the position and (*hkl*) indices of the Bragg reflections from the hexagonal lattice. The horizontal white dashed lines in the contour plot indicates the melting of the ionic superstructure.

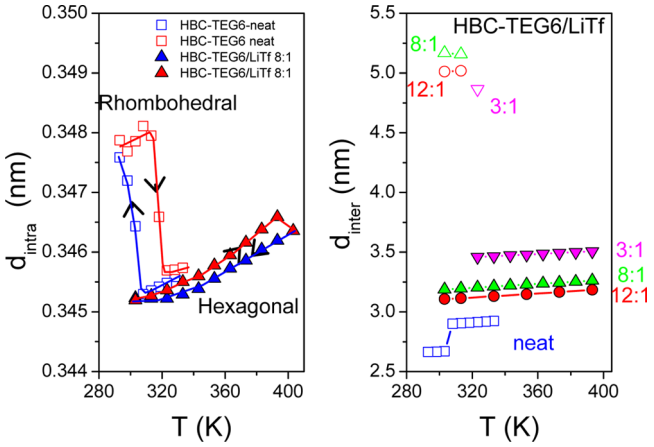

Figure 6. (left) Temperature dependence of intracolumnar spacing for neat HBC-TEG6 (squares) and HBC-TEG6/LiTf with [EO]:[Li$^+$] ratio 8:1 (triangles). Red and blue symbols indicate data obtained on heating and cooling, respectively. (right) Temperature dependence of domain spacing along the intercolumnar direction for neat HBC-TEG6 (blue squares); HBC-TEG6/LiTf at three concentrations: [EO]:[Li$^+$] = 12:1 (red circles), 8:1 (green up triangles), and 3:1 (magenta down-triangles) on cooling.

agreement with the ones from DSC. Discotic liquid crystals within their columnar arrangement have anisotropic interactions: van der Waals between the columns and $\pi-\pi$ within the columns. This anisotropy in molecular interactions gives rise to anisotropic thermodynamic properties, as for example, in thermal expansion which now depends on directionality.[20] From the temperature dependence of the first equatorial and of the more intense meridional reflection the inter- and intramolecular distances can be extracted associated respectively with inter- and intracolumnar correlations. In the bulk, the thermal expansion coefficients associated with the intercolumnar correlations within the hexagonal and rhombohedral lattices correspond to $\alpha^{H}_{inter} = 3.06 \times 10^{-4}$ K^{-1} and $\alpha^{R}_{inter} = 1.38 \times 10^{-4}$ K^{-1}, respectively. From the intracolumnar correlations, a weaker temperature dependence is obtained with $\alpha^{H}_{intra} = 4.9 \times 10^{-5}$ K^{-1} and $\alpha^{R}_{intra} = 3.3 \times 10^{-5}$ K^{-1} in accord with the smaller thermal expansion coefficient found in graphite ($\sim 2.5 \times 10^{-5}$ K^{-1}).[20]

The self-assembly in the presence of salt is distinctly different and is discussed with respect to Figures 5 and 6. The WAXS patterns (Figure 5) at low and higher temperatures indicate peaks associated with the (100), (110), and (200) reflections from a hexagonal unit cell. In addition, a weak equatorial reflection and additional meridional reflections appear at lower temperatures (T = 303 K in Figure 5). Addition of salt has two effects; first, it stabilizes the high-temperature hexagonal structure found in the bulk and, second, induces a reversible transition at temperatures around 333 K associated with an ionic superstructure (see below). These effects are discussed with respect to the temperature dependence of the intra- and intercolumnar spacings.

Figure 6 depicts only a minor change of the intracolumnar spacing and a major increase of intercolumnar distances with the addition of salt. Within the hexagonal lattice, intercolumnar distances increase from 2.9 nm in the neat compound **4** to ~3.5 nm in the electrolyte with the higher salt concentration. This reveals that ions are incorporated exclusively within the intercolumnar space which is a prerequisite for a good ionic conductor. In addition, an ionic superstructure is formed as indicated by the weak equatorial reflection (corresponding distance of ~5 nm) and weak meridional reflections (corresponding distances of 0.41 and 0.37 nm). Since ionic correlations exceed the intercolumnar spacing, they could suggest an ionic superstructure that surrounds the columns in the form of a helix with correlation distances of ~5 and 0.41 nm between and along the columns, respectively. This is schematically depicted in Figure 7. The lack of sufficient reflections from the ionic superstructure precludes a more definite structural assignment. Nevertheless, ions are spatially correlated in a superstructure that surrounds the HBC columns and further stabilize the hexagonal lattice from higher temperatures. Below it will be explored how this ionic superstructure affects the ionic conductivity.

Ionic Conductivity. The dc ionic conductivity was extracted from the plateau in σ' both for the neat compound **4** and for the HBC-TEG6 doped with LiTf with salt concentrations [EO]:[Li$^+$] = 12:1, 8:1, and 3:1. In the neat compound **4**, conductivity is some 2 orders of magnitude lower than in the doped systems (Figure S8). This reflects the presence of some ionic impurities of in the neat compound (despite efforts to remove ions with water). The temperature dependence of the dc conductivity in the doped system is plotted in Figure 8 on cooling and subsequent heating. On cooling, and for temperatures below (above) the formation of the ionic superstructure, $\sigma'_{dc}(T)$ exhibits a Vogel–Fulcher–Tammann (Arrhenius) T dependence. Instead, during heating, two VFT dependencies are required: one at temperatures below and one above the melting temperature of the superstructure. In addition, in samples with salt concentrations [EO]:[Li$^+$] = 12:1 and 8:1, there is a discontinuous increase of

DOI: 10.1021/acs.macromol.7b00224
Macromolecules XXXX, XXX, XXX–XXX

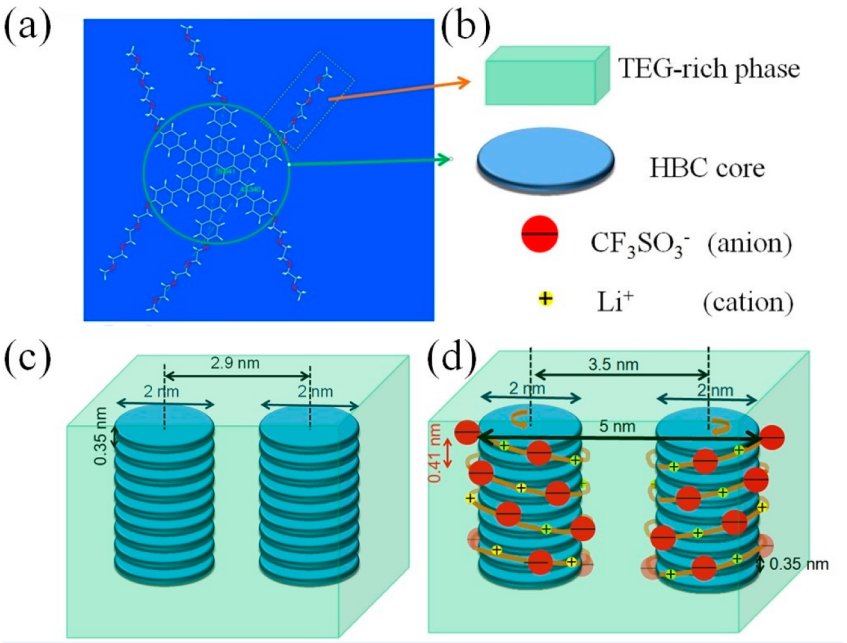

Figure 7. Schematic representations of (a) neat HBC-TEG6, (b) its constituents, (c) the columnar arrangement of neat HBC-TEG6, and (d) the HBC-TEG6 columnar organization in the presence of salt with salt concentration [EO]:[Li^+] = 3:1.

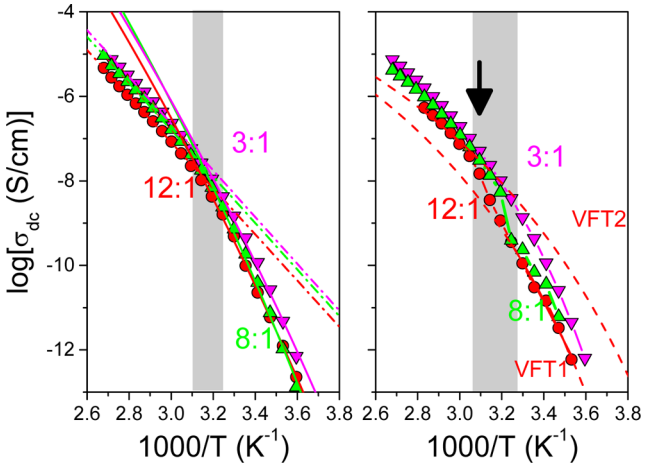

Figure 8. The dc conductivity of HBC-TEG6/LiTf at different [EO]:[Li^+] ratios: 12:1 (spheres), 8:1 (up triangles), and 3:1 (down triangles) during cooling (left) and during heating (right). The gray areas indicate the transition region. The black arrow indicates the melting of the ionic superstructure. The solid and dash-dotted lines represent fits to the Arrhenius and VFT equations, respectively.

$\sigma'_{dc}(T)$ by about an order of magnitude at the melting of the ionic superstructures. This fact demonstrates the detrimental role of the ionic superstructure on ion conduction. There is some analogy of the ionic superstructure in doped HBCs with the complex crystal formed in the archetypical polymer electrolyte composed of linear PEG chains doped with LiTf.[29,37−39] In both cases, complexation impedes ion transport and reduces the dc conductivity. A recent study demonstrated a switching of ionic conductivity in wedge-shaped liquid crystalline ammonium salts.[10] In this case the conductivity in the hexagonal columnar phase was several orders of magnitude higher than in the rectangular columnar phase.

In addition to the ionic superstructure, the HBC columnar organization may also impede ionic motion. To explore this effect, we compare the dc conductivities of the linear TEG chains with the ones in HBC-TEG6 doped with LiTf at the same salt concentrations. The comparison is shown in Figure S9. In HBC-TEG6/LiTf, the normalized dc conductivity with respect to the TEG/LiTf content is reduced by 1−2 orders of magnitude, suggesting that the HBC columnar structures perturb the conformation of TEG chains and effectively increase the viscosity for ion transport. Therefore, there are two factors that control ionic conductivity in the doped HBCs: the HBC columnar structures that on one hand provide the required rigidity (see below) but reduce ionic conductivity, on the other, and the ionic superstructure that further reduces the ionic conductivity. Evidently, both structural features lead to a higher effective viscosity (see below with respect to the viscoelastic properties). Nevertheless, columnar structures are an important element of electronic conduction. Below we will consider ways to circumvent formation of the ionic superstructure.

Local Dynamics. Dielectric spectroscopy, apart from affording the ionic conductivity, provides access to the local dipolar dynamics in the bulk and doped system. Some representative dielectric loss curves for the neat and doped compound **4** are shown in Figure 9. In **4**, three dielectrically active processes exist, that one at lower temperatures corresponds to the local γ- and β-processes and at higher temperatures to the α-process that effectively carries most of the dielectric strength. At lower frequencies/higher temperatures the mechanism of ionic conductivity originating from ionic impurities is also apparent from the steep rise of dielectric loss.

The origin of these dynamics in DLCs has been the subject of combined efforts by dielectric spectroscopy with site-specific NMR techniques.[23,24] It was shown that the α-process reflects the in- and out-of-plane reorientation of the disks within the columnar structures. This dynamic process is cooperative in nature as reflected in the distribution of relaxation times (with low- and high-frequency shape parameters of $m \sim 0.5$ and $mn \sim$

DOI: 10.1021/acs.macromol.7b00224
Macromolecules XXXX, XXX, XXX−XXX

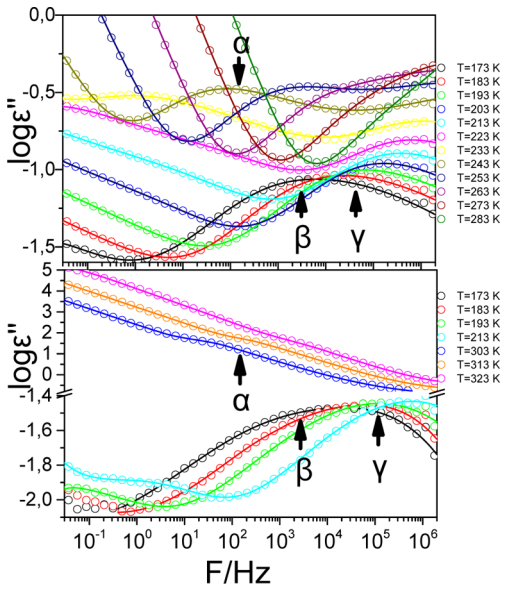

Figure 9. (top) Dielectric loss curves of neat HBC-TEG6 at some selected temperatures as indicated. The lines represent the result of a fit using two HN functions and the conductivity contribution. The different dynamic processes are indicated as α, β, and γ. (bottom) Dielectric loss curves of HBC-TEG6/LiTf with salt concentration [EO]:[Li$^+$] = 8:1 at some selected temperatures as indicated. The lines are fits to a summation of HN functions together with the conductivity contribution.

0.24) and in the temperature dependence of the associated relaxation times (Figure 10). The $\tau(T)$ dependence conforms to a VFT dependence

$$\tau = \tau_0 \exp\left(\frac{B}{T - T_0}\right) \quad (5)$$

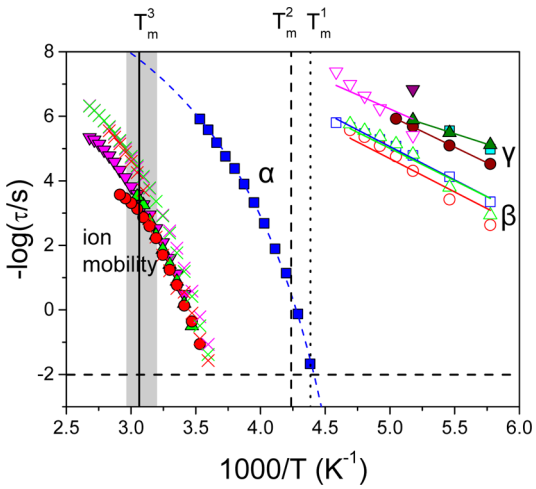

Figure 10. Temperature dependence of the relaxation times of the α-process (filled symbols), β-process (open symbols), and γ-process (filled symbols) on inverse temperature of HBC-TEG6 neat (squares), HBC-TEG6/LiTf with salt concentration [EO]:[Li$^+$] = 12:1 (circles), HBC-TEG6/LiTf with [EO]:[Li$^+$] = 8:1 (up-triangles), and HBC-TEG6/LiTf with [EO]:[Li$^+$] = 3:1 (down-triangles). The dashed and solid lines represent fits to the VFT and Arrhenius equations, respectively. The vertical solid, dashed, and dash-dotted lines indicate the melting temperatures from DSC.

Here, τ_0 (=10^{-12} s) is the limiting relaxation time at very high temperatures, B (=1400 ± 20 K) is the activation parameter, and T_0 (=183.2 ± 0.7 K) is the "ideal" glass temperature, located below the glass temperature, T_g (=227 ± 1 K) the latter defined as the temperature where the α-relaxation times is at 100 s. On the contrary, the $\tau(T)$ dependence for the β- and γ-processes is Arrhenius-like with similar activation energies of ~39.6 ± 0.1 kJ/mol. These processes reflect local fluctuations of ethylene glycol within the glassy state.

Doping with LiTf alters significantly the local dynamics as indicated in the dielectric loss curves of HBC-TEG6/LiTf with salt concentration [EO]:[Li$^+$] = 8:1 (Figure 9) (the dielectric loss spectra are compared in Figure S10). Figure 9 depicts similar local dynamics (β and γ) below the glass temperature associated with the ethylene oxide dipoles as in bulk compound **4** but distinctly different slower dynamics. Now the α-process is coupled to the motion of ions. This is shown in Figure 10, where the relaxation times for the α-process are compared with the characteristic times associated with the mechanism of ionic conduction. First, both mechanisms have a VFT temperature dependence. Second, the two mechanisms are coupled, meaning that the motion of ions within the ionic superstructure and the reorientation of disks are concerted.[19,23,24] This highly cooperative process is also reflected in the broader distribution of relaxation times in the doped systems.

Viscoelastic Properties. Application of materials as alternatives to solid polymer electrolytes requires a high modulus as to prevent dendritic growth at the electrodes.[30] The viscoelastic properties of the HBC-TEG6 doped with LiTf at salt concentration [EO]:[Li$^+$] = 3:1 was studied with rheology, and the storage and loss shear moduli are shown in Figure 11 as a function of temperature under isochronal

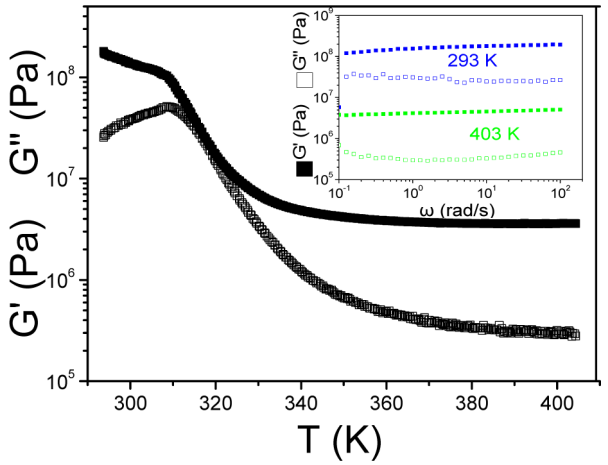

Figure 11. Temperature dependence of storage (filled symbols) and loss (open symbols) moduli for HBC-TEG6/LiTf with [EO]:[Li$^+$] = 3:1 obtained during heating at a frequency of 10 rad/s with rate of 2 K/min. Inset: storage (filled symbols) and loss (open symbols) moduli at 293 and 403 K. At both temperatures the sample exhibits viscoelastic behavior.

conditions. They depict an elastic response at temperatures below and above melting of the ionic superstructure, with respective values of storage moduli of ~10^8 and ~10^6 Pa. In particular, the high value of the storage modulus at room temperature (G' ~ 10^8 Pa) reflects the presence of the columnar structure *and* of the ionic superstructure.

DOI: 10.1021/acs.macromol.7b00224
Macromolecules XXXX, XXX, XXX−XXX

At higher temperatures, melting of the ionic superstructure gives a viscoelastic solid with a modulus of ($G' \sim 10^6$ Pa) that is constant over a broad temperature range. At such temperatures ionic conductivity is maximized. More information on the viscoelastic state is provided by frequency sweeps performed at different temperatures (293 and 403 K) corresponding to temperatures below and above melting of the ionic superstructure. At both temperatures they indicate a viscoelastic solid with relatively high moduli, a prerequisite for battery applications. At this point it would be interesting to explore means of further increasing dc conductivity by e.g. suppressing the propensity for an ionic superstructure, while maintaining a high modulus.

*Effect of Asymmetric PEG Substitution (Compound **8**).* A way to explore this possibility is by desymmetrization of the model compound **4**, e.g., by employing the same HBC building block but substituted with only two PEG chains (compound **8**). In this case, PEG with a molecular weight of 750 g/mol was used due to solubility reasons. Attachment of only two PEG chains is expected to break the symmetry of the ionic superstructure. This conjecture is confirmed by comparing the DSC traces of the neat compound **8** with the same compound doped with LiTf (Figure 12). The DSC traces of

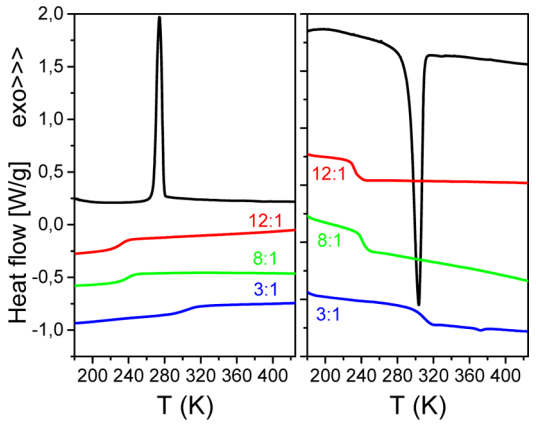

Figure 12. DSC traces of neat compound **8** (black) and of the same compound doped with LiTf at different salt concentrations:[EO]:[Li$^+$] = 12:1 (red), 8:1 (green), and 3:1 (blue). Traces are obtained during the second cooling (left) and the second heating run (right) with a rate of 10 K/min. Traces are shifted vertically for clarity.

neat **8** indicate a crystallization/melting peak associated with the crystalline structure of PEG. This structure as well as any other superstructure are absent in the traces of the doped compound with [EO]:[Li$^+$] = 12:1 and 8:1 salt concentrations. The presence of a step in the heat flow at the respective glass temperature further confirms that these systems are completely amorphous.

Moreover, there is an increasing glass temperature with increasing LiTf content (at 231, 240, and 309 K for [EO]:[Li$^+$] salt concentrations of 12:1, 8:1, and 3:1, respectively). Only in [EO]:[Li$^+$] = 3:1 salt concentration there exists a small endothermic peak at 372 K ($\Delta H \sim 0.4$ J/g). This situation in the doped compound **8** is distinctly different from compound **4** with the strong ionic superstructure. (The self-assembly of the neat compound **8** is discussed with respect to Figure S11.)

The effect of desymmetrization on the ionic conductivity is discussed with respect to Figure 13. The figure depicts dc conductivities for the doped compound **8** with salt concentration [EO]:[Li$^+$] = 12:1 being about an order of magnitude higher than in compound **4** with the same salt concentration. Furthermore, the $\sigma(T)$ dependence displays a VFT temperature dependence over a broad temperature associated with the amorphous nature of the systems. Lastly, the higher ionic conductivity is more evident by plotting the normalized ionic conductivity with respect to the corresponding linear PEG chains. In the inset to Figure 13, the normalized conductivity is less than a decade lower as compared to the linear PEG chains. This shows that desymmetrization suppresses the propensity for formation of an ionic superstructure and facilitates ionic conduction.

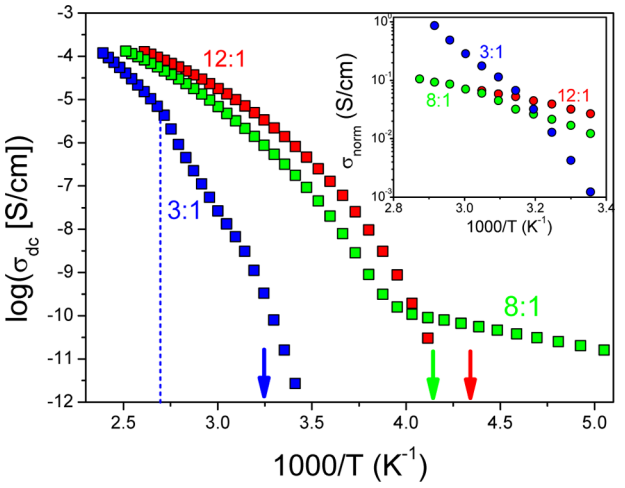

Figure 13. The dc conductivity of compound **8** at different [EO]:[Li$^+$] ratios 12:1 (red squares), 8:1 (green squares), and 3:1 (blue squares). The vertical line indicates the melting temperature of the complex for the 3:1 ratio. The solid lines represent fits to the VFT equation. The vertical dashed line gives the melting of the weak structure in [EO]:[Li$^+$] = 3:1. Vertical arrows give the respective glass temperatures. The inset gives the normalized conductivities relative to the corresponding linear PEG chains.

In addition to ionic conductivity, electronic conductivity measurements of compound **4** are currently in progress.

IV. CONCLUSION

Ion conductive liquid crystals show great potential as new electrolytes because they provide efficient conductive pathways for ion transport. Furthermore, liquid crystals composed of flat hydrocarbon cores with enhanced π-stacking and hydrophilic chains that can solvate lithium salts and are mobile at ambient temperature are possible candidates of materials that combine electronic and ionic transport. Discotic liquid crystals based on HBCs substituted with short PEG chains were synthesized and doped with LiTf. Structural analysis revealed nanophase-separated domains composed from HBC cores organized in columns surrounded by PEG chains. The columns were further organized in rhombohedral and hexagonal lattices at lower and higher temperatures, respectively. In analogy with the crystalline complex formed in the archetypical PEG/LiTf electrolyte, ions in PEG-functionalized HBCs are spatially correlated forming an ionic superstructure. Structural analysis demonstrated that ions are incorporated exclusively within the PEG domain, surround the HBC columns, and follow the disks in their rotational motion. Furthermore, ions stabilize the hexagonal lattice from higher temperatures. Because of the presence of the columnar structures and the ionic super-

DOI: 10.1021/acs.macromol.7b00224
Macromolecules XXXX, XXX, XXX−XXX

structure, the electrolyte behaves as a viscoelastic solid with a high shear modulus ($G' \sim 10^8$ Pa) at ambient temperature. However, the presence of the ionic superstructure impedes ion motion. At temperatures higher than the melting of the ionic superstructure, ionic conductivity increases by an order of magnitude to a value of 10^{-5} S/cm. As a means of suppressing the ionic superstructure we have explored the desymmetrization effect on HBC functionalization e.g. with only two PEG chains in the disk periphery. Asymmetric PEG substitution breaks the symmetry of the ionic superstructure and increases ionic conductivity by another order of magnitude while retaining a high shear modulus ($G' \sim 5 \times 10^6$ Pa) and a viscoelastic response. These findings demonstrate that PEG-functionalized HBCs have great potential as new electrolytes because they combine high ionic conductivity with mechanical stability through the mobile PEG phase and HBC columnar structures, respectively.

Ionic conduction can be combined with electronic conduction. Efforts in this direction could pave the way for the construction of molecular devices based on HBC-PEG coaxial structures that best combine electronic *and* ionic pathways.

■ ASSOCIATED CONTENT

Supporting Information

The Supporting Information is available free of charge on the ACS Publications website at DOI: 10.1021/acs.macromol.7b00224.

Sample preparation methods, ionic conductivity, structural relaxation times and structure analysis of compound **8** (PDF)

■ AUTHOR INFORMATION

Corresponding Author

*(G.F.) E-mail gfloudas@uoi.gr.

ORCID

Klaus Müllen: 0000-0001-6630-8786

George Floudas: 0000-0003-4629-3817

Notes

The authors declare no competing financial interest.

■ ACKNOWLEDGMENTS

The current work was supported by the Research unit on Dynamics and Thermodynamics of the UoI cofinanced by the European Union and the Greek state under NSRF 2007-2013 (Region of Epirus, call 18).

■ REFERENCES

(1) Riess, I. Mixed Ionic-Electronic Conductors − Material Properties and Applications. *Solid State Ionics* **2003**, *157*, 1−17.

(2) Riess, I. Review of the Limitations of the Hebb-Wagner Polarization Method for Measuring Partial Conductivities in Mixed Ionic Electronic Conductors. *Solid State Ionics* **1996**, *91*, 221−232.

(3) Costantini, N.; Wegner, G.; Mierzwa, M.; Pakula, T. Simultaneous Ionic and Electronic Conductivity in Polymeric Materials. *Macromol. Chem. Phys.* **2005**, *206*, 1345−1354.

(4) Witker, D.; Curtis, M. D. Lithium Ion and Electronic Conductivity in 3-(oligoethylene oxide) thiophene Comb-Like Polymers. *J. Power Sources* **2006**, *156*, 525−532.

(5) Patel, S. N.; Javier, A. E.; Stone, G. M.; Mullin, S. A.; Balsara, N. P. Simultaneous Conduction of Electronic Charge and Lithium Ions in Block Copolymers. *ACS Nano* **2012**, *6*, 1589−1600.

(6) Patel, S. N.; Javier, A. E.; Stone, G. M.; Mullin, S. A.; Balsara, N. P. Simultaneous Electronic and Ionic Conduction in a Block Copolymer: Applications in Lithium Battery Electrodes. *Angew. Chem., Int. Ed.* **2011**, *50*, 9848−9851.

(7) Högberg, D.; Soberats, B.; Uchida, S.; Yoshio, M.; Kloo, L.; Segawa, H.; Kato, T. Nanostructures Two-component Liquid-Crystalline Electrolytes for High-Temperature Dye-Sensitized Solar Cells. *Chem. Mater.* **2014**, *26*, 6496−6502.

(8) Sakuda, J.; Hosono, E.; Yoshio, M.; Ichikawa, T.; Matsumoto, T.; Ohno, H.; Zhou, H.; Kato, T. Liquid-Crystalline Electrolytes for Lithium-Ion Batteries: Ordered Assemblies of a Mesogen-Containing Carbonate and a Lithium Salt. *Adv. Funct. Mater.* **2015**, *25*, 1206−1212.

(9) Soberats, B.; Yoshio, M.; Ichikawa, T.; Ohno, H.; Kato, T. Zwitterionic Liquid Crystals as 1D and 3D Lithium Ion Transport Media. *J. Mater. Chem. A* **2015**, *3*, 11232−11238.

(10) Soberats, B.; Yoshio, M.; Ichikawa, T.; Zeng, X.; Ohno, H.; Ungar, G.; Kato, T. Ionic Switch Induced by a Rectangular-Hexagonal Phase Transition in Benzenammonium Columnar Liquid Crystals. *J. Am. Chem. Soc.* **2015**, *137*, 13212−13215.

(11) Boden, N.; Bushby, R. J.; Clements, J. Mechanism of Quasi-one-dimensional Electronic Conductivity in Discotic Liquid Crystals. *J. Chem. Phys.* **1993**, *98*, 5920−5931.

(12) van de Craats, A. M.; Warman, J. M.; Fechtenkötter, A.; Brand, J. D.; Harbison, M. A.; Müllen, K. Record Charge Carrier Mobility in a Room-Temperature Discotic Liquid-Crystalline Derivative of Hexabenzocoronene. *Adv. Mater.* **1999**, *11*, 1469−1472.

(13) van de Craats, A. M.; Warman, J. M. The Core-size Effect on the Mobility of Charge in Discotic Liquid Crystalline Materials. *Adv. Mater.* **2001**, *13*, 130−133.

(14) van de Craats, A. M.; Warman, J. M. Charge Mobility in Discotic Materials Studied by PR-TRMC. Mol. *Mol. Cryst. Liq. Cryst.* **2003**, *396*, 41−72.

(15) Pisula, W.; Kastler, M.; Wasserfallen, D.; Mondeshki, M.; Piris, J.; Schnell, I.; Müllen, K. Relation between Supramolecular Order and Charge Carrier Mobility of Branched Alkyl Hexa-*peri*-hexabenzocoronenes. *Chem. Mater.* **2006**, *18*, 3634−3640.

(16) Pisula, W.; Menon, A.; Stepputat, M.; Lieberwirth, I.; Kolb, U.; Tracz, A.; Sirringhaus, H.; Pakula, T.; Müllen, K. A Zone-Casting Technique for Device Fabrication of Field-Effect Transistors Based on Discotic Hexa-peri-hexabenzoeoronene. *Adv. Mater.* **2005**, *17*, 684−689.

(17) Feng, X.; Marcon, V.; Pisula, W.; Hansen, M. R.; Kirkpatrick, J.; Grozema, F.; Andrienko, D.; Kremer, K.; Müllen, K. Towards High Charge-Carrier Mobilities by Rational Design of the Shape and Periphery of Discotics. *Nat. Mater.* **2009**, *8*, 421−426.

(18) Hill, J. P.; Jin, W.; Kosaka, A.; Fukushima, T.; Ichihara, H.; Shimomura, T.; Ito, K.; Hashizume, T.; Ishii, N.; Aida, T. Self-Assembled Hexa-*peri*-hexabenzocoronene Graphitic Nanotube. *Science* **2004**, *304*, 1481−1483.

(19) Haase, N.; Grigoriadis, C.; Butt, H.-J.; Müllen, K.; Floudas, G. Effect of Dipole Functionalization on the Thermodynamis and Dynamics of Discotic Liquid Crystals. *J. Phys. Chem. B* **2011**, *115*, 5807.

(20) Grigoriadis, C.; Haase, N.; Butt, H.-J.; Müllen, K.; Floudas, G. Negative Thermal Expansion in Discotic Liquid Crystals of Nanographenes. *Adv. Mater.* **2010**, *22*, 1403−1406.

(21) Grigoriadis, C.; Haase, N.; Butt, H.-J.; Müllen, K.; Floudas, G. To Tilt or Not to Tilt? Kinetics of Structure Formation in a Discotic Liquid Crystal. *Soft Matter* **2011**, *7*, 4680−4689.

(22) Papadopoulos, P.; Grigoriadis, C.; Haase, N.; Butt, J.-J.; Müllen, K.; Floudas, G. Dynamics of Structure Formation in a Discotic Liquid Crystal by Infrared Spectroscopy and Related Techniques. *J. Phys. Chem. B* **2011**, *115*, 14919−14927.

(23) Elmahdy, M. M.; Floudas, G.; Mondeshki, M.; Spiess, H. W.; Dou, X.; Müllen, K. Origin of the Complex Molecular Dynamics in Functionalized Discotic Liquid Crystals. *Phys. Rev. Lett.* **2008**, *100*, 107801.

DOI: 10.1021/acs.macromol.7b00224
Macromolecules XXXX, XXX, XXX−XXX

(24) Hansen, M. R.; Feng, X.; Macho, V.; Müllen, K.; Spiess, H. W.; Floudas, G. Fast and Slow Dynamics in a Discotic Liquid Crystal with Regions of Columnar Order and Disorder. *Phys. Rev. Lett.* **2011**, *107*, 257801.
(25) Duran, H.; Hartmann-Azanza, B.; Steinhart, M.; Gehrig, D.; Laquai, F.; Feng, X.; Müllen, K.; Butt, H.-J.; Floudas, G. Arrays of Aligned Supramolecular Wires by Macroscopic Orientation of Columnar-Discotic Mesophases. *ACS Nano* **2012**, *6*, 9359.
(26) Lee, M.; Kim, J.-W.; Peleshanko, S.; Larson, K.; Yoo, Y.-S.; Vaknin, D.; Markutsya, S.; Tsukruk, V. V. *J. Am. Chem. Soc.* **2002**, *124*, 9121−9128.
(27) Wu, J.; Li, J.; Kolb, U.; Müllen, K. *Chem. Commun.* **2006**, 48−50.
(28) Gilding, D. K.; Reed, A. M. Reed, Biodegradable Polymers for Use in Surgery-Poly(ethylene oxide) poly(ethylene terephthalate) (PEO/PET) Copolymers. A.M. *Polymer* **1979**, *20*, 1454−1458.
(29) Zardalidis, G.; Ioannou, E.; Pispas, S.; Floudas, G. Relating Structure, Viscoelasticity and local Mobility to Conductivity in PEO/LiTf Electrolytes. *Macromolecules* **2013**, *46*, 2705−2714.
(30) Monroe, C.; Newman, J. The Impact of Elastic Deformation on Deposition Kinetics at Lithium/Polymer Interfaces. *J. Electrochem. Soc.* **2005**, *152*, A396−A404.
(31) Gomez, E. D.; Panday, A.; Feng, E. H.; Chen, V.; Stone, G. M.; Minor, A. M.; Kisielowski, C.; Downing, K. H.; Borodin, O.; Smith, G. D.; Balsara, N. P. Effect of Ion Distribution of Conductivity of Block Copolymer Electrolytes. *Nano Lett.* **2009**, *9*, 1212−1216.
(32) Yuan, R.; Teran, A. A.; Gurevitch, I.; Mullin, S. A.; Wanakule, N. S.; Balsara, N. P. Ionic Conductivity of Low Molecular Weight Block Copolymer Electrolytes. *Macromolecules* **2013**, *46*, 914−921.
(33) Panday, A.; Mullin, S.; Gomez, E. D.; Wanakule, N.; Chen, V. L.; Hexemer, A.; Pople, J.; Balsara, N. P. Effect of Molecular Weight and Salt Concentration on Conductivity of Block Copolymer Electrolytes. *Macromolecules* **2009**, *42*, 4632−4637.
(34) Young, W.-S.; Epps, T. H., III. Salt Doping in PEO-Containing Block Copolymers: Counterion and Concentration Effects. *Macromolecules* **2009**, *42*, 2672−2678.
(35) Young, W.-S.; Kuan, W.-F.; Epps, T. H., III Block Copolymer Electrolytes for Rechargeable Lithium Batteries. *J. Polym. Sci., Part B: Polym. Phys.* **2014**, *52*, 1−16.
(36) Teran, A. A.; Balsara, N. P. Thermodynamics of Block Copolymers with and without Salt. *J. Phys. Chem. B* **2014**, *118*, 4−17.
(37) Zardalidis, G.; Gatsouli, K.; Pispas, S.; Mezger, M.; Floudas, G. Ionic Conductivity, Self-Assembly, and Viscoelasticity in Poly(styrene-*b*-ethylene oxide) Electrolytes Doped with LiTf. *Macromolecules* **2015**, *48*, 7164−7171.
(38) Zardalidis, G.; Ioannou, E. F.; Gatsouli, D. K.; Pispas, S.; Kamitsos, E. I.; Floudas, G. Ionic Conductivity and Self-assembly in Poly(isoprene-*b*-ethylene oxide) Electrolytes doped with LiTf and EMITf. *Macromolecules* **2015**, *48*, 1473−1482.
(39) Zardalidis, G.; Pipertzis, A.; Mountrichas, G.; Pispas, S.; Mezger, M.; Floudas, G. Effect of Polymer Architecture on the Ionic Conductivity. Densely Grafted Poly(ethylene oxide) Brushes Doped with LiTf. *Macromolecules* **2016**, *49*, 2679−2687.
(40) Broser, W.; Reusch, J.; Kurreck, H.; Siegle, P. *Chem. Ber.* **1969**, *102*, 1715−1724.
(41) Wunderlich, K.; Grigoriadis, C.; Zardalidis, G.; Klapper, M.; Graf, R.; Butt, H.-J.; Müllen, K.; Floudas, G. Poly(ethylene glycol)-functionalized Hexaphenylbenzenes as Unique Amphiphiles: Supramolecular Organization and Ion Conductivity″. *Macromolecules* **2014**, *47*, 5691−5702.
(42) Lee, M.; Kim, J.-W.; Peleshanko, S.; Larson, K.; Yoo, Y.-S.; Vaknin, D.; Markutsya, S.; Tsukruk, V. V. *J. Am. Chem. Soc.* **2002**, *124*, 9121−9128.
(43) Kremer, F.; Schönhals, A. *Broadband Dielectric Spectroscopy*; Springer: Berlin, 2002.
(44) Floudas, G. Dielectric Spectroscopy. In *Polymer Science: A Comprehensive Reference*; Matyjaszewski, K., Möller, M., Eds.; Elsevier BV: Amsterdam, 2012; Vol. 2.32, pp 825−845.
(45) Floudas, G.; Paluch, M.; Grzybowski, A.; Ngai, K. *Molecular Dynamics of Glass-Forming Systems: Effects of Pressure*; Springer Science & Business Media: 2010; Vol. *1*.
(46) Havriliak, S.; Negami, S. A complex Plane Representation of Dielectric and Mechanical Relaxation Processes in Some Polymers. *Polymer* **1967**, *8*, 161−210.

DOI: 10.1021/acs.macromol.7b00224
Macromolecules XXXX, XXX, XXX−XXX